Local-Ising-type magnetic order and metamagnetism in the rare-earth pyrogermanate $Er_2Ge_2O_7$

K. M. Taddei,[1,*] L. Sanjeewa,[2,3] J. W. Kolis,[3] A. S. Sefat,[2] C. de la Cruz,[1] and D. M. Pajerowski[1]
[1]*Neutron Scattering Division, Oak Ridge National Laboratory, Oak Ridge, Tennessee 37831, USA*
[2]*Materials Science and Technology Division, Oak Ridge National Laboratory, Oak Ridge, Tennessee 37831, USA*
[3]*Department of Chemistry, Clemson University, Clemson, South Carolina 29634, USA*

(Received 30 September 2018; revised manuscript received 30 November 2018; published 11 January 2019)

The recent discoveries of proximate quantum spin-liquid compounds and their potential application in quantum computing informs the search for new candidate materials for quantum spin-ice and spin-liquid physics. While the majority of such work has centered on members of the pyrochlore family due to their inherently frustrated linked tetrahedral structure, the rare-earth pyrogermanates also show promise for possible frustrated magnetic behavior. With the familiar stoichiometry $R_2Ge_2O_7$, these compounds generally have tetragonal symmetry with a rare-earth sublattice built of a spiral of alternating edge and corner-sharing rare-earth site triangles. Studies on $Dy_2Ge_2O_7$ and $Ho_2Ge_2O_7$ have shown tunable low temperature antiferromagnetic order, a high frustration index, and spin-ice-like dynamics. Here we use neutron diffraction to study magnetic order in $Er_2Ge_2O_7$ (space group $P4_12_12$) and find the lowest yet Neél temperature in the pyrogermanates of 1.15 K. Using neutron powder diffraction, we find the magnetic structure to order with $k = (0, 0, 0)$ ordering vector, magnetic space group symmetry $P4_1'2_12'$, and a refined Er moment of $m = 8.1\ \mu_B$ near the expected value for the Er^{3+} free ion. Provocatively, the magnetic structure exhibits similar "local Ising" behavior to that seen in the pyrocholres where the Er moment points up or down along the short Er-Er bond. Upon applying a magnetic field, we find a first-order metamagnetic transition at ~0.35 T to a lower symmetry $P2_1'2_1'2$ structure. This magnetic transition involves an inversion of Er moments aligned antiparallel to the applied field describing a class I spin-flip-type transition, indicating a strong local anisotropy at the Er site—reminiscent of that seen in the spin-ice pyrochlores.

DOI: 10.1103/PhysRevMaterials.3.014405

I. INTRODUCTION

Magnetically frustrated materials have long drawn enthusiasm from the condensed matter community for their ability to strain familiar approximations, reveal new physics, and host exotic ground states [1–3]. This particular combination of attributes leads frustrated magnetic materials, at times, to present an accessible interface between condensed matter theory and experiment, where relatively simple, or at least enumerable, Hamiltonians are able to describe the rich physics observed [1,2,4]. Indeed, an early test system for commercially produced quantum computers has been frustrated spin glasses for this reason [5]. This interface has been reinvigorated recently with the discovery of proximate quantum spin-liquid materials and the ostensible vitality of frustrated quantum magnetic states for quantum computing, bringing anew interest in the discovery of new frustrated materials [6–13].

Historically, one of the most fruitfully studied families of frustrated magnetic materials has been the rare-earth pyrochlores ($R_2B_2O_7$ with R = La–Yb, B = Ti, Ge, Sn) [4,14–17]. With a structural motif of corner-sharing R tetrahedra which naturally give rise to competing exchange interactions, these systems tend to complex frustrated magnetic ground states such as spin ices, glasses, and liquids, and consequently reveal emergent novel physics [18–20]. In members such as $Dy_2Ti_2O_7$ and $Ho_2Ti_2O_7$, the local ion anisotropy forces the R site magnetic moment to point along the R tetrahedron's local ⟨111⟩ direction [15,19]. This defines a local form of the Ising model where each R site can point parallel or antiparallel to the local ⟨111⟩ axis mapping to the spin-up/spin-down Ising description [15]. When the ferromagnetic (FM) exchange interaction between neighboring R sites is considered the famous spin-ice rule state is achieved, which describes a strong frustration that confounds long-range magnetic order down to the lowest measured temperatures of several mK [15,21].

In the R pyrochlores, the large magnetic moment of the R site suggests that dipole-dipole interactions can contribute significantly to the magnetic Hamiltonian in addition to the exchange interaction, crystal field effects, and spin-orbit coupling [4]. Therefore, tuning the relative strength of the different magnetic interactions—and, consequently, the level of frustration—is possible and easily achieved through changing the R ion (and consequently the magnetic moment size and crystal field levels) or the application of an external magnetic field [22,23]. Such effects have been systematically studied and result in discrete changes in appropriate magnetic interaction models between neighboring Lanthanides (such as Ising for $Dy_2Ti_2O_7$ and XY for $Er_2Ti_2O_7$) and even low field magnetic transitions under applied field (metamagnetic transitions [MMT]) [22–25]. In this way, a phase diagram can be created where tuning the relative strengths of the

*Corresponding author: taddeikm@ornl.gov

exchange and dipole-dipole interactions leads to a phase space with numerous possible magnetic ground states—including exotic frustrated states. Such tuning is easily controlled with experimental conditions (such as pressure or applied field) or via changing the incorporated *R* and thus allows for tuning from traditional long-range magnetic order to exotic magnetic states [26].

The interest and success of the pyrochlores in revealing new physics informs a search for similar materials whose properties might beget similar competing magnetic interactions. The *R* pyrogermanates (REPG) share the pyrochlore's stoichiometry but with a lower symmetry nuclear structure (as low as space group $P\bar{1}$). Nonetheless, these systems also exhibit an inherently geometrically frustrated *R* structural motif built of a spiral structure with alternating corner sharing and edge sharing *R* triangles [27].

Despite this potential, little work has been performed on the REPG family. Beyond the intial synthesis report, only the $Ho_2Ge_2O_7$, $Dy_2Ge_2O_7$, and $Er_2Ge_2O_7$ members of the REPG family have received further study [28–30]. These members crystallize with the tetragonal space group $P4_12_12$ and exhibit highly anisotropic magnetic susceptibilities. In $Ho_2Ge_2O_7$ (for which neutron diffraction data has been reported), below 1.6 K magnetic ordering is seen with a large magnetic moment of 9 μ_B/Ho and complex magnetic structure with the Ho moments locked in the crystallographic *ab* plane and rotating along the *c* axis [28]. Interestingly, in both the $Dy_2Ge_2O_7$ and $Ho_2Ge_2O_7$ materials, field-dependent ac susceptibility measurements suggest the rare-earth ions behave like Ising-spins with spin-relaxation phenomena which indicate similar magnetic behavior to the spin-ice pyrochlores [18,23,31–33].

In this paper, we report neutron scattering studies on the $Er_2Ge_2O_7$ REPG down to mK temperatures. Our work finds magnetic order below 1.15 K with a three-dimensional spiral structure unlike the coplanar structure reported in $Ho_2Ge_2O_7$. This ordering temperature is well below that predicted from Curie-Weiss fitting of the high temperature magnetic susceptibility, suggesting significant frustration. Upon application of a small (<1 T) external magnetic field, we find $Er_2Ge_2O_7$ undergoes a MMT. Single-crystal neutron diffraction reveals that with the field applied in the easy plane of the $Er_2Ge_2O_7$ material, the MMT is of spin-flip type with moments antiparallel to the applied field inverting through their crystallographic site. These results suggest a similarity between the *R*PG and the *R* pyrochlores with a similar geometric frustration and strong competition between different magnetic interaction mechanisms.

II. EXPERIMENTAL METHODS

A. Synthesis

Single crystals of $Er_2Ge_2O_7$ were synthesized using a direct combination of Er_2O_3 and GeO_2 via high temperature and high pressure hydrothermal synthesis. In a typical reaction, 0.4 g of total reactants (0.2981 g of HEFA rare earth 99.99% Er_3O_2 and 0.1019 g of Alfa Aesar 99.9% GeO_2) were used in 4:5 stoichiometric ratio. The crystalline products were grown at 650 °C for 14 days in fine silver (99.9%) $3/8'' \times 2.5''$ ampules loaded into a Tuttle cold seal autoclave constructed from Inconel 718 material. The ampules were loaded with the appropriate component oxides and weld sealed from both ends after addition of 0.8 mL of 20 M CsF as a mineralizer. Upon reaction completion, the silver ampules were opened and washed with deionized water. The yield of $Er_2Ge_2O_7$ single crystals was ∼90% with the remainder being unreacted powder. Single crystals of $Er_2Ge_2O_7$ were produced as pink plate-shaped crystals approximately $1 \times 1 \times 0.5$ mm in size.

Powder samples of $Er_2Ge_2O_7$ were synthesized using a conventional solid state method. A mixture of total mass 5 g (3.2323 g Er_2O_3 and 1.7677 g GeO_2)was used with a stoichiometric ratio of 1:2. The reactants were mixed, ground, and heat to 1000 °C for 12 h. The resultant powders were pressed into pellets and calcined at 1250 °C for 1 day. To ensure homogeneity, several reheating and regrinding steps were performed until no further impurities were present in the sample.

Initial characterization of the single-crystal and powder samples were carried out via room temperature single-crystal and powder x-ray diffraction using a Bruker D8 Venture with Incoatec Mo K_α microfocus source Photon 100 CMOS detector and a Rigaku Ultima IV diffractometer with CuK_α radiation, respectively. The collected single-crystal data was processed and scaled using the Apex3 (SAINT and SADABS) software suites and Rietveld refinements were performed using the SHELXTL software suite [34].

Magnetization measurements were carried out using a magnetic property measurement system (Quantum Design) using finely ground crystals of $Er_2Ge_2O_7$. Temperature-dependent data were collected upon warming in a magnetic field of 10 kOe. Isothermal magnetization versus applied field curves were collected at 2 K.

B. Neutron scattering experiments

Neutron powder diffraction measurements were performed on the HB-2A (POWDER) beamline of Oak Ridge National Laboratory's High Flux Isotope Reactor. Approximately 4.5 g of powder $Er_2Ge_2O_7$ were placed into an aluminum powder can sealed under helium atmosphere. Field- and temperature-dependent measurements were performed using a cryomagnet loaded with a 3He cryostick, allowing for field and temperature ranges of 0–5 T and 0.5–300 K, respectively.

Diffraction patterns were collected on HB-2A using the open-21′-12′ collimator settings (for premonochromator, presample, and predetector collimation, respectively) with both the short wavelength, high-intensity 1.54 Å and longer wavelength "magnetism-optimized" 2.41 Å monochromator reflections. Powder patterns were collected over a scattering vector (Q) range of 0.09 Å^{-1} < Q < 4.63 Å^{-1} with count times between 1 and 8 hours per scan. For temperature-dependent scans of peak intensities, a detector was positioned to be centered in 2θ on the peak position and then the temperature was increased as scattering rates counts were taken using counting times of 200 s/T.

Analysis of the neutron powder diffraction data was performed using the Rietveld method as implemented in the FullProf software suite [35]. The Thompson-Cox-Hasting formulation for a pseudo-Voight peak shape with axial divergence asymmetry was used to fit the instrumental profile of HB-2A

[36]. In addition to profile fitting, the atomic positions, atomic displacement parameters of all sites as well as the fractional occupancies were refined. For magnetic structure determination, the Simulated Annealing and Representational Analysis (SARAh) and ISODISTORT software programs were used [37,38]. Visualization of the crystal structure was performed using VESTA [39].

Single-crystal neutron-diffraction measurements were performed on the HB-1 and HB-3 triple-axis beamlines of HFIR with use of cryomagnet loaded with a 3He insert. Due to the small size of the as-grown crystals, three crystals were coaligned for measurement totaling 3.8 mg. The crystals were mounted on an aluminum pin with a small amount of varnish and the pin was masked with Gd_2O_3 to minimize contamination from scattering off the aluminum mount. The alignment of the crystals and the geometry of the triple axis spectrometers allowed access to the $H0L$ scattering plane. To maximize flux, loose collimation was used with the $\lambda = 2.36$ Å 14.7 meV incident beam.

III. RESULTS AND DISCUSSION

A. Structure

$Er_2Ge_2O_7$ is reported to crystallize with the tetragonal noncentrosymmetric $P4_12_12$ space group symmetry [27]. Our studies corroborate these results as seen in Fig. 1(a), which shows a neutron powder diffraction pattern of $Er_2Ge_2O_7$ collected under ambient conditions modeled with the reported $P4_12_12$ structure. The model produces a satisfactory agreement with the data with R_{wp} and χ^2 parameters of 10.0 and 2.69, respectively. We note that while visually the fit looks quite good, we obtain a larger than expected R_{wp}. We attribute this to the significant region of the fit ($Q < 2$ Å^{-1}) which consists mainly of a large sloping background. This feature of the data will be discussed more later. The obtained refinement parameters for the 300, 2, and 0.5 K data are reported in Table I.

The refined structure of $Er_2Ge_2O_7$ is shown in Figs. 1(b)–1(d). As enumerated in Table I, the $P4_12_12$ structure has one independent crystallographic site each for Er and Ge but four independent sites for the O atoms, three of whose site symmetry places no restrictions on the x,y,z positions. This leads to significantly different A and B site O coordination than in the pyrochlores. In the RPG, the A-site is coordinated by seven surrounding oxygen rather than eight, creating a highly distorted pentagonal bipyramid rather than the distorted cube [Fig. 1(b)]. Due to the low symmetry of the O sites, the bonding within the ErO_7 bipyraminds is highly variable ranging from ∼2.21 to ∼2.37 Å. The pentagonal bipyramids are edge sharing creating a continuous Er helix along the c direction. The B-site Ge atoms are tetrahedrally coordinated by O and form corner-sharing tetrahedron [Fig. 1(b)] with bond lengths between ∼1.78 and ∼1.74 Å.

Along the tetragonal axis, the Er sublattice can be divided into four layers each with two Er which stack to create a spiral, wrapping around the c axis [Figs. 1(b) and 1(c)]. In analogy to the pyrochlores, we can also consider how the Er are self-coordinated. As shown in Fig. 1(d), the Er form a unit of edge sharing triangles which are bent along the short axis.

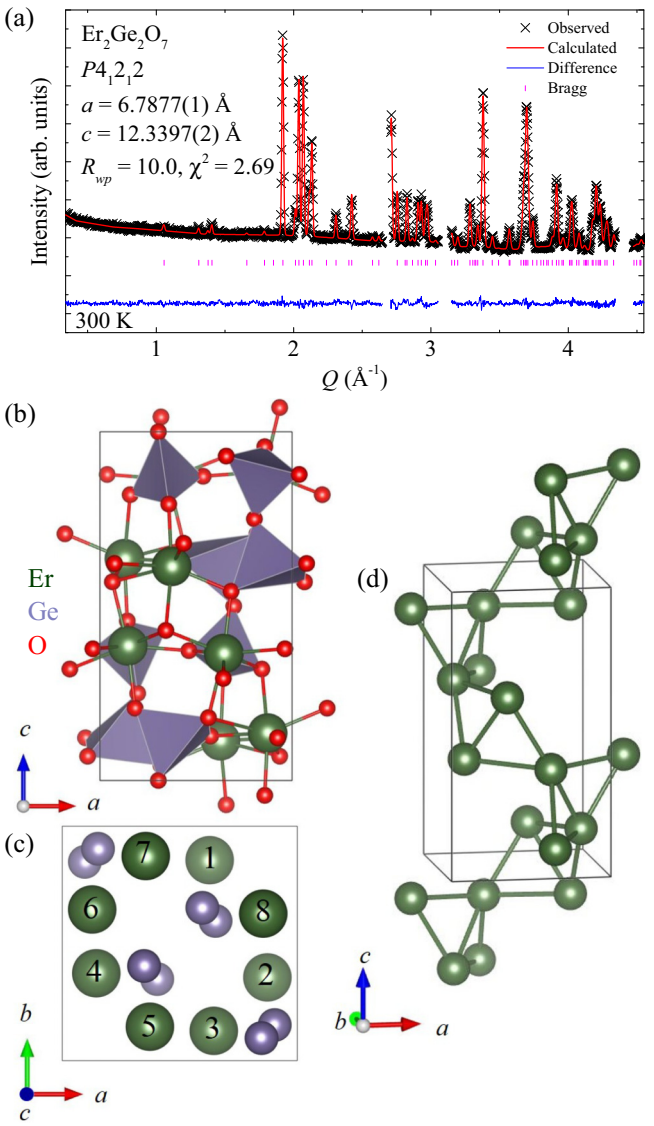

FIG. 1. (a) Neutron diffraction pattern and Rietveld refinement of $Er_2Ge_2O_7$ with space group symmetry $P4_12_12$, data collected at 300 K with an incident beam of 2.41 Å. (b) $P4_12_12$ structure with Er, Ge, and O atoms in green, purple, and red, respectively. (c) View of unit cell along the c axis with O atoms removed for clarity. Er sites are numbered in sets per layer so that atoms 1 and 2 describe the bottom layer and so on—these labels are not consistent with the atom labels from symmetry operations. (d) Er sublattice highlighting the alternating edge and corner sharing sharing Er_3 triangle unit (e). Gaps in the diffraction pattern shown in panel (a) are regions containing Al peaks from the sample can which have been excluded from the refinement.

These units are then linked through corner sharing alternately along their short and long axes, creating the Er sublattice helix. This structure was also well-described in Ref. [28] for the $Ho_2Ge_2O_7$ RPG member.

Compared to $Ho_2Ge_2O_7$ structurally, we find $Er_2Ge_2O_7$ to have slightly reduced a and c lattice parameters with a reduction of ∼0.3% in each direction. This contraction of the unit cell is consistent with the slightly smaller ionic radius of Er^{3+} and results in a slight contraction of the in-plane and

TABLE I. Crystallographic parameters of $Er_2Ge_2O_7$ at 300, 2, and 0.5 K. Parameters determined from Rietveld refinements performed using the 300, 2, and 0.5 K data collected with the 1.54 $Å^{-1}$ wavelength. The atomic displacement parameters and magnetic moment are reported in units of $Å^2$ and μ_B/Er, respectively.

		300 K	2.0 K	0.5 K
Space group		$P4_12_12$	$P4_12_12$	$P4_12_12$
R_{wp}		7.17	9.40	8.29
χ^2		1.96	3.79	3.10
a (Å)		6.7877(1)	6.7829(1)	6.7826(1)
c (Å)		12.3397(2)	12.3319(2)	12.3317(3)
c/a		1.8180(2)	1.8181(2)	1.8181(2)
V ($Å^3$)		568.52(1)	567.36(3)	567.30(3)
Er (8a)				
	x	0.8770(3)	0.8741(4)	0.8743(4)
	y	0.3553(3)	0.3547(5)	0.3545(4)
	z	0.1354(2)	0.1358(2)	0.1360(2)
	U	0.0054(6)	0.0027(9)	0.00060(8)
	M			8.1(3)
Ge (8a)				
	x	0.9014(3)	0.9001(5)	0.9008(6)
	y	0.1534(3)	0.1514(5)	0.1508(6)
	z	0.6197(2)	0.6188(3)	0.6181(3)
	U	0.0068(5)	0.0060(9)	0.0091(1)
O1 (4a)				
	x	0.8045(4)	0.8038(6)	0.8028(8)
	y	0.1956(4)	0.1962(6)	0.1972(8)
	z	0.75	0.75	0.75
	U	0.013(1)	0.0065(2)	0.015(3)
O2 (8a)				
	x	0.0786(5)	0.0769(7)	0.0744(8)
	y	−0.0327(4)	−0.0321(6)	−0.0318(7)
	z	0.6233(3)	0.6242(4)	0.6247(5)
	U	0.0072(8)	0.0036(1)	0.0039(1)
O3 (8a)				
	x	0.0639(4)	0.0648(6)	0.0663(8)
	y	0.3399(6)	0.3379(9)	0.337(1)
	z	0.5710(3)	0.5709(4)	0.5719(5)
	U	0.010(9)	0.009(1)	0.01(2)
O4 (8a)				
	x	0.6828(4)	0.6844(6)	0.6839(8)
	y	0.1409(5)	0.1439(7)	0.1458(9)
	z	0.5436(2)	0.5449(4)	0.5456(4)
	U	0.010(8)	0.0054(1)	0.0049(1)

out-of-plane R-R distances as well as the R-O bond lengths [40]. However, no significant broader changes are seen in either the Er sublattice or in the ErO_7 polyhedron. As will be discussed in Sec. III C, the magnetic interactions in the RPG are expected to be complex with competing interactions. This 0.3% contraction then gives a possible tuning parameter—or an additional effect to consider—in the determination of magnetic order. Here, the R sites are brought closer together, which naively should increase dipole-type interactions between the anticipated large magnetic moments on these sties.

Diffraction patterns were collected at 300, 2, 1.2, 0.8, and 0.5 K allowing minimal tracking of the lattice parameters' temperature dependencies. As shown in Table I, between 2 and 300 K both the a and c lattice parameters dilate, as expected for thermal expansion. The measure of the expansion's anisotropy is obtained by taking the ratio c/a. From 300 to 2 K, the c/a ratio shows no change within the certainty of our measurements, indicating an isotropic contraction.

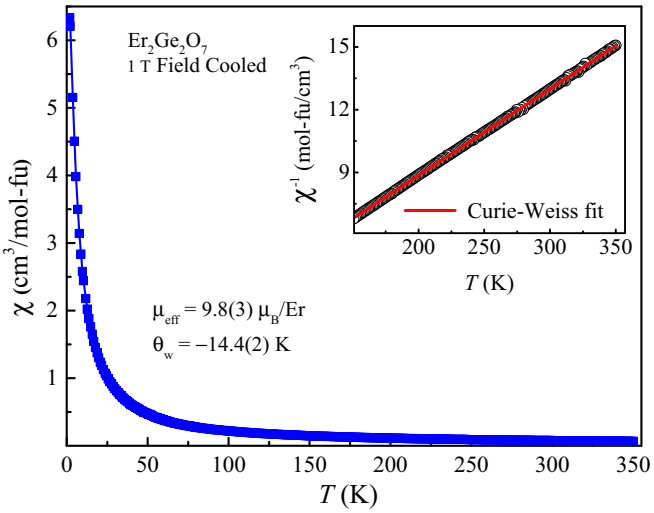

FIG. 2. Susceptibility measurements performed on powder sample of $Er_2Ge_2O_7$ under a 1 T field following a field-cooling procedure. Fitting of the inverse susceptibility shown in the inset was performed using the standard Curie-Weiss law $\chi^{-1} = C(T - \theta_w)$.

B. Zero-field magnetic structure

While previous reports on the $Dy_2Ge_2O_7$ and $Ho_2Ge_2O_7$ RPG found evidence of magnetic order in transport measurements and solved the magnetic structure using neutron diffraction, respectively, no magnetic order has yet been reported in $Er_2Ge_2O_7$ [28,29]. Early work measuring the anisotropic susceptibility suggested possible order with a Curie-Weiss temperature (θ_w) of ∼6 K [30]. However, no report the authors are aware of has measured down to these temperatures, leaving it an open question as to whether $Er_2Ge_2O_7$ exhibits long-range magnetic order—and at what temperature. Such information is important in studying magnetic frustration in the RPG and how it is tuned as the R moves across the Lanthanide period.

To build on the results of Ghosh *et al.*, (Ref. [30]), we performed susceptibility measurements on a powder sample of $Er_2Ge_2O_7$ (Fig. 2). We observe no evidence of magnetic ordering down to 2 K. Above ∼100 K, typical Curie-Weiss behavior is seen as reported for both $Ho_2Ge_2O_7$ and $Dy_2Ge_2O_7$. To facilitate comparison with the Dy and Ho analogues, we perform Curie-Weiss fitting as described in Refs. [28,29], e.g., fitting the inverse susceptibility with $\chi^{-1} = C(T - \theta_w)$ over the range 120 K $\leqslant T \leqslant$ 300 K. From our fit, we obtain an effective magnetic moment of $\mu_{\text{eff}} = 9.8(3)\mu_B$/Er and a Weiss temperature of $\theta_w = -14.4(2)$ K. We find a negative Weiss temperature indicative of antiferromagnetic (AFM) interactions in agreement with Ghosh *et al.* [30]. However, the absolute value of our Weiss temperature is larger than previously reported, we attribute this to the finer temperature steps and higher temperature cutoff (120 K) used in our

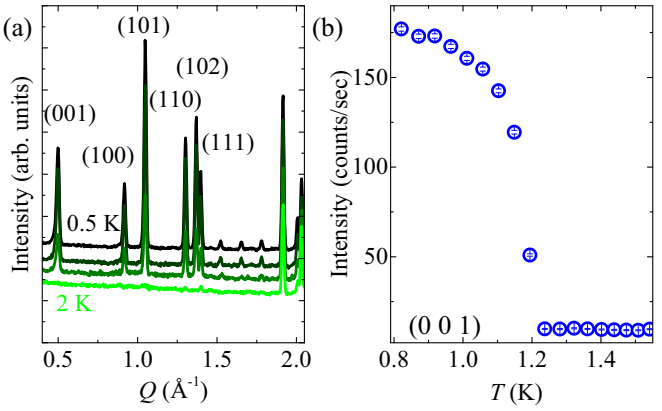

FIG. 3. (a) Waterfall of neutron diffraction patterns collected at 2, 1.2, 0.8, and 0.5 K. (b) Temperature dependence of new low temperature (001) reflection collected on single-crystal sample.

analysis, the former of which allows for the range of linear behavior to be more carefully determined [30].

In Fig. 1(a), we noted an uncharacteristically large low-Q background signal, which monotonically gains intensity with decreasing Q. Such a signal is similar to that expected from the magnetic form factor of local moments in a paramagnetic state—in this case, the Er^{3+} $4f$ electrons [41]. At 2 K, this signal is still present with a slightly increased count rate. As the material is cooled below 1.2 K, a series of new low Q peaks appear and the previously high background drops [Fig. 3(a)]. Upon further cooling, the intensity of the new peaks grows until saturating at ~0.8 K, behavior indicative of magnetic ordering. Figure 3(b) shows the temperature dependence of the 0.5 $Å^{-1}$ peak, which may be fit with a power law $(M(T)\alpha(T - T_N)^{\beta})$, revealing the transition temperature to be ~1.15 K.

The drop in paramagnetic background at the ordering temperature and temperature dependence of the peak intensity are consistent with a magnetic origin to the signal. We therefore attempt to account for the new peaks with a magnetic model using representational analysis, starting with the identification of an ordering vector. In this case, the numerous new low Q peaks can be indexed with the nuclear unit cell indicating an ordering vector of $k = (0, 0, 0)$ [Fig. 3(a)]. Using the SARAh software, the irreducible representations (Γ) consistent with the $P4_12_12$ space group symmetry and a $k = (0, 0, 0)$ ordering vector were generated and are shown in Table II with the Γ in Miller and Love notation [38] (for a complete description of the Γ and constituent basis vectors (ψ) see the Supplemental Material (SM) [42]). Five Γ were found, giving rise to seven possible magnetic structures. Γ_1, Γ_2, Γ_3, and Γ_4 each have three independent ψ, leading to three refinable parameters per structure—two for the ab plane and one for the moment along the c lattice direction. Γ_5 has twelve ψ which can be subdivided by symmetry, leading to three possible structures in the Γ_5 representation, one of which is the low symmetry linear combination of all twelve ψ. Due to the exceptional increase in refinable parameters of this model, we remove it from our considerations.

Figure 4 shows the six remaining magnetic structures enumerated in Table II. In earlier work on $Ho_2Ge_2O_7$, Morosan *et.*

TABLE II. Irreducible representations (Γ), magnetic space groups, magnetic supercell, number of basis vectors (ψ), and fit parameters for Rietveld refinements using 0.5 K data for magnetic orderings with $k = (000)$. The the low-symmetry $P2_1'$ model was not considered due to its significant increase in the number of refinable parameters.

Γ	Magnetic space group	ψ	R_{wp}	χ^2
Γ_1 ($mGM1$)	$P4_12_12$	3	48.6	76.8
Γ_2 ($mGM2$)	$P4_1'2_12'$	3	9.76	3.10
Γ_3 ($mGM3$)	$P4_12_1'2'$	3	49.8	80.7
Γ_4 ($mGM4$)	$P4_12_1'2$	3	52.3	88.9
Γ_5 ($mGM5$)	$P2_1'2_1'2$	6	39.6	51.0
	$C22'2_1'$	6	40.4	53.3
	$P2_1'$	12		

al. reported the $mGM1$ representation as accurately modeling the 1.36 K magnetic structure [28]. They determined an in-plane spiral structure with a 90° rotation between R planes. A version of this structure with an out-of-plane component is shown in the first panel of Fig. 4.

In Table II, we report the fit residuals from Rietveld refinements using the 0.5 K data for each of the magnetic structures. The strong (100) and (110) peaks in Fig. 3 indicate the presence of significant out-of-plane magnetic moment in $Er_2Ge_2O_7$. Consequently, the in-plane Γ_1 model is incapable of adequately modeling our diffraction data. Even when an out-of-plane component is added, Γ_1 results in a $R_{wp} > 40$ (we note that a fit to the 0.5 K data with no magnetic structure results in R_{wp} and χ^2 of 64.7 and 136, respectively). Similarly, the Γ_3, Γ_4, and Γ_5 models result in poor fits, with R_{wp} never reaching <30. Rather convincingly, we find the Γ_2 structure with magnetic space group symmetry $P4_1'2_12'$ to produce the best fit parameters with $R_{wp} = 9.76$ and $\chi^2 = 3.10$.

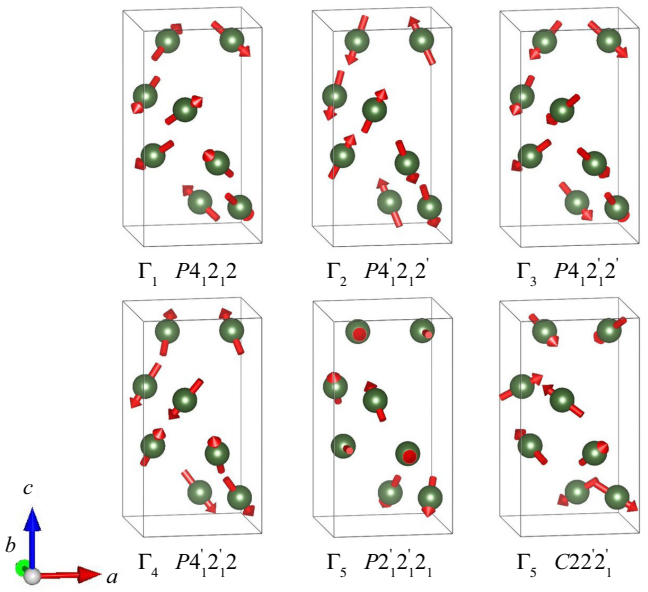

FIG. 4. Possible magnetic structures with $k = (0, 0, 0)$ enumerated in Table II. The values of the basis vectors where determined from attempted fitting of the 0.5 K neutron powder diffraction data.

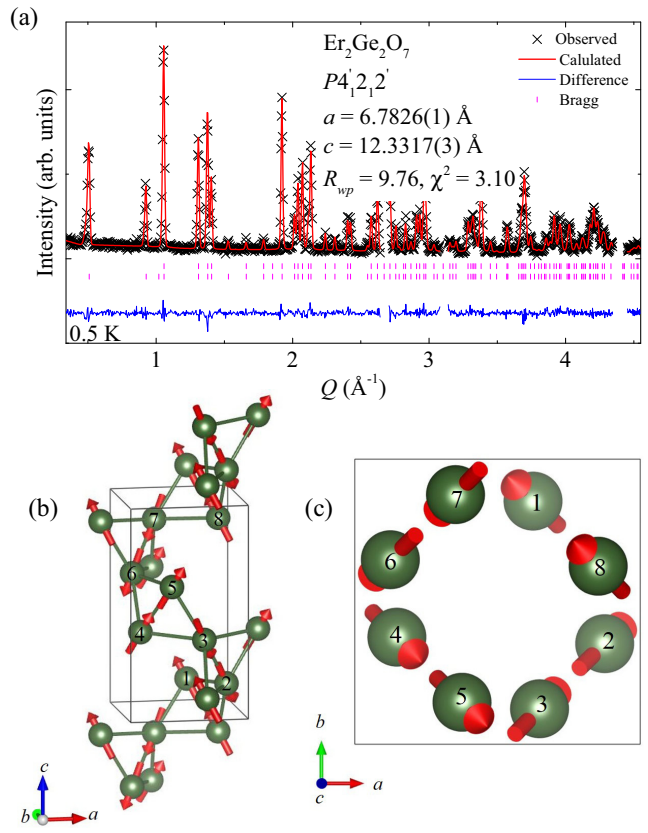

FIG. 5. (a) Rietveld refinement using 0.5 K data and the magnetic structure generated by Γ_2. Refined magnetic structure with Er atoms labeled as described in Fig. 1 viewed along the (b) ab plane and along the (c) c axis.

The resulting fit is shown in Fig. 5(a) producing a visually excellent agreement with the data. The fit Γ_3 structure requires nonzero contributions from all three ψ (two in-plane and one along the c axis) and leads to the three-dimensional magnetic structure seen in Figs. 5(b) and 5(c). Considering the previously discussed Er edge-sharing sublattice, we find the magnetic structure has FM correlations along the edge-sharing Er-Er bond with the moment pointing along the bond direction. As the edge-sharing triangles are rotated to construct the full Er sublattice, we find AFM correlations along c between neighboring units and alternating FM and AFM correlations along the a and b directions, creating a right-handed spiral [Fig. 5(b)] with no net magnetization.

In this structure, the Er moments exhibit a kind of "local Ising" behavior, where the moments are either spin-up or spin-down along the shortest and edge-sharing bond in the triangular Er sublattice. Notably, this is similar to the magnetic order of the spin-ice pyrochlores, where a large local anisotropy forces the R moments to point along the local ⟨111⟩ direction either into or out of the R tetrahedra [15,21]. Interestingly, it is this configuration which leads to the spin-ice rules in the prochlores. As will be discussed more later, the observation of a similar local Ising behavior indicates similar physics in $Er_2Ge_2O_7$.

Our refinements produce a magnetic moment of $8.1(3)\mu_B/Er$ with $m_a = 2.66(4)$, $m_b = 3.03(3)$ and $m_c = -6.98(4)\mu_b$/Er. For elemental tripositive Er (Er^{3+}), which has total angular momentum J of $\frac{15}{2}$, the theoretical saturated magnetic moment is $9\mu_B$/Er—close to our refined value. We note that unlike $Ho_2Ge_2O_7$, the moment size obtained from Curie-Weiss fitting and predicted by the theory of rare-earth magnetism agrees reasonably well with our refined magnetic moment.

Using the $\theta_w = -14.4$ K together with $T_N = 1.15$ K, we can determine the frustration index $f = |\theta_W|/T_N \sim 13$, indicating significant frustration [3,43]. This is higher than the $f \sim 6$ and 2 found for $Ho_2Ge_2O_7$ and $Dy_2Ge_2O_7$, respectively [28,29]. With a motif of edge sharing triangles, the Er sublattice might be expected to show frustrated behavior; however, as was the case in $Ho_2Ge_2O_7$, the frustration is apparently alleviated by the formation of a spiral magnetic structure.

Despite being isostructural, we find that the magnetic behavior in the *R*PG as the R is changed from Dy to Ho to Er somewhat complex. For all three, the reported magnetic moment has been near the saturated free-ion expectation (∼10.5, 9.1 and 8.1 μ_B, respectively) [28,29]. Furthermore, the magnetic ordering temperature follows a similar trend, decreasing with decreasing moment size from 2.2 to 1.6 to 1.15 K. Although the crystallographic parameters of the Dy compound are not reported, the decrease in T_N correlates with the lattice contraction anticipated for the reduction in ionic radius from Dy to Ho to Er [40]. Interestingly, the θ_w follows the opposite trend, reaching a maximum absolute value of 14.4 K for the Er compound and decreasing to 9.6 and 4.4 K for Ho and Dy, respectively [28–30].

Considering the complex dynamic magnetic behavior reported in both $Ho_2Ge_2O_7$ and $Dy_2Ge_2O_7$ which indicated multiple competing interactions and timescales, it is unsurprising that simple moment size considerations are inadequate here for predicting the bulk magnetic behavior in these compounds. It is likely necessary to understand how the crystal field levels and dipole-dipole interactions change as the lanthanide is exchanged to accurately predict the magnetic behavior. It should be expected that subtle changes to the RO_7 local environment due to lattice contraction and differences between the valance orbitals of Dy, Ho, and Er should affect the crystal field levels and local anisotropy directions.

C. Field dependence of the magnetic structure

In light of the strong field-dependent behavior reported for both $Ho_2Ge_2O_7$ and $Dy_2Ge_2O_7$, neutron diffraction patterns of $Er_2Ge_2O_7$ were collected under an applied field [28,29]. In a powder sample, such study is useful as a first approach to determine field dependence and critical values, though the random orientation of the crystallites in the powder suggests that the measured state is likely a mixture of different states.

Figure 6(a) shows powder diffraction patterns collected at 0.5 K under fields of 0, 0.35, 1, 2, and 4 T. At the lowest applied field of 0.35 T, changes in the intensities of the magnetic peaks are observed, with a series of reflections [e.g., (001), (100), and (102)] losing intensity. As the field is increased to 4 T, these reflections continue to monotonically decrease in intensity. At 4 T the (001), (100), and (102) reflections are almost entirely suppressed with integrated intensities less than 10% of their zero-field value. Simultaneously, the

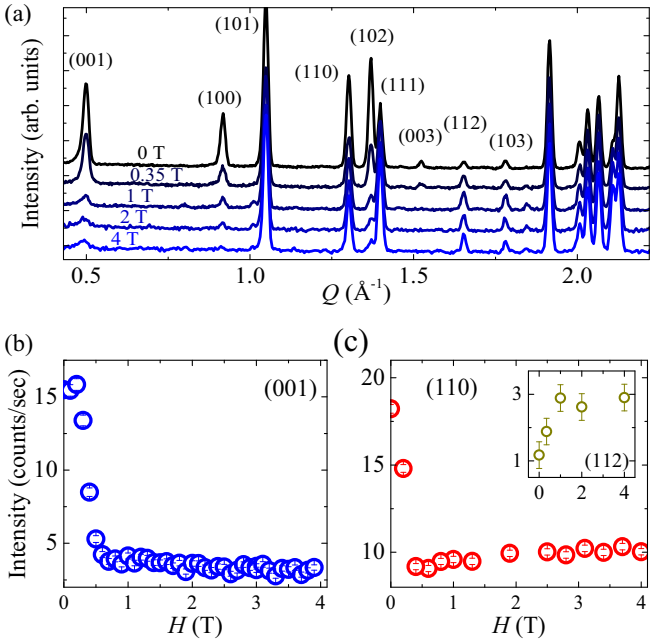

FIG. 6. (a) Waterfall of neutron diffraction patterns collected at 0.5 K under 0, 0.35, 1, 2, and 4 T applied fields. Field dependence of the (b) (001) and (c) (110) peak intensities. The inset of panel (c) shows the peak intensity for the (112) reflection integrated from the diffraction patterns shown in panel (a). All panels are of diffraction data collected using powder samples.

(111), (112), and (103) reflections gain intensity for $H > 0$ T. These reflections increase monotonically as the applied field is increased to 4 T [Fig. 6(a)].

The increasing/decreasing intensity of different species of reflections indicates the applied field is driving a magnetic transition and not simply suppressing the magnetic order. However as seen in Fig. 6(a), no new reflections arise under field. Therefore, the new structure must share the original $k = (0, 0, 0)$ ordering vector. Figures 6(b) and 6(c) show order parameter scans for the (001) and (110) reflections performed as a function of applied field. For the (001) reflection, the peak intensity steeply drops showing critical behavior with a transition field of $H_c \sim 0.5$ T. Similarly, albeit on a coarser field grid, the (110) reflection is quickly suppressed and nearly constant by 0.5 T again showing critical behavior. These observations suggest a true phase transition. Considering the k vector, we should expect the new magnetic structure to select a different irreducible representation (irrep) or combination of irreps from Table II (Fig. 4).

Such a field-driven magnetic transition can be characterized as a MMT and should result from a reorientation of the spin directions in response to the applied field and the anisotropies of the magnetic site [44]. This could result in either a spin-flip transition, where the moments undergo a 180° change in polarization along the direction of the applied field, or a spin-flop transition where the moments rotate in response to the field. The former outcome is expected for a material with strong anisotropies while the latter is suggestive of weaker anisotropies [44]. Therefore, characterization of the resulting magnetic structure would give information about the anisotropy of the rare-earth site. However, this is not possible

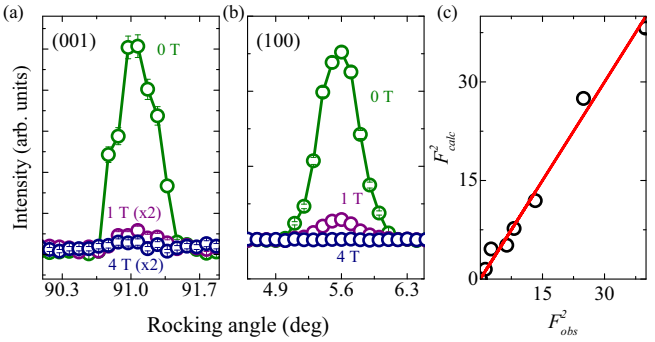

FIG. 7. Single-crystal data showing rocking curves on the (a) (001) and (b) (100) magnetic reflections under applied fields of 0, 1 and 4 T. (c) Calculated peak intensities (F^2_{calc}) plotted as a function of the observed intensities (F^2_{obs}) for Rietveld refinements using the $P2'_12'_12$ magnetic structure to model the single crystal data collected under a 4 T applied field.

with powder diffraction data for reasons described previously and so motivates single-crystal neutron-diffraction study.

We note that the behavior of the order parameters shown in Figs. 6(b) and 6(c) above H_c is perhaps not quite constant as one would expect. We attribute this to the lack of orientation to the applied field due to the polycrystalline nature of the powder sample. A field-driven transition in a system with high anisotropy should be dependent on the direction of the applied field [15]. Therefore, it is possible we are averaging over different field-induced magnetic structures, or seeing other effects due to a "misaligned" field [15].

Single-crystal neutron diffraction was performed to elucidate the field-dependent magnetic structure. Geometrical considerations of the experimental setup limited access of reciprocal space to a single (HKL) plane perpendicular to the applied field. The choices of scattering plane and field direction where therefore limited. The previous work on $Dy_2Ge_2O_7$ and $Ho_2Ge_2O_7$ identified the easy axis as in the ab plane [28,29]. Furthermore, our neutron powder diffraction data demonstrated $(H00)/(0K0))$ and $(00L)$ type peaks as responding strongly to field. Therefore, we chose to align our applied field with the crystallographic a direction and probe a $(H0L)$ cut of reciprocal space [28,29].

Figures 7(a) and 7(b) show the field dependence of the (001) and (100) magnetic reflections, respectively. In agreement with our powder results, both peaks are suppressed by the applied field with the largest intensity changes between 0 and 1 T. As for the powder experiment, with increasing field both reflections are monotonically suppressed. In the single crystal, however, the intensities of these peaks are more strongly suppressed and by 4 T both are background equivalent.

To perform Rietveld refinements, rocking curves were collected on ∼25 nuclear and magnetic reflections under applied fields of 0, 1, and 4 T. The integrated intensities were then used to model the possible magnetic structures allowed by the $k = (000)$ ordering vector (Fig. 4). Due to the relative scarcity of peaks, the nuclear structure was fixed at the crystallographic properties determined from the low temperature zero field powder measurements. As a check, we modeled the zero field structure and confirmed the results of

TABLE III. Irreducible representations, magnetic space groups and fit parameters for single-crystal Rietveld refinements for data collected at 0.5 K under applied fields of 1 and 4 T. The irrep labels are consistent with those presented in Table II.

		$R_{wF^2}(\chi^2)$	
Γ	Magnetic space group	1 T	4 T
Γ_1 ($mGM1$)	$P4_12_12$	79.0(11.5)	99.8(16.0)
Γ_2 ($mGM2$)	$P4_1^{'}2_12^{'}$	45.9(3.87)	87.5(14.0)
Γ_3 ($mGM3$)	$P4_12_1^{'}2^{'}$	42.5(3.31)	77.4(11.0)
Γ_4 ($mGM4$)	$P4_12_1^{'}2$	36.0(2.38)	61.2(6.87)
Γ_5 ($mGM5$)	$P2_1^{'}2_1^{'}2$	27.9(2.30)	13.9(0.62)
	$C22^{'}2_1^{'}$	31.2(2.04)	44.9(3.69)

our powder studies finding the Γ_2 irrep as producing the best fit ($R_{wF^2} \sim 14\%$).

The resulting fit residuals for fits to the 1 and 4 T data are shown in Table III. Starting with the 4 T data, we find the Γ_2 model is no longer able to reproduce the measured intensities indicating, as suggested by the order parameter scans, the sample has undergone a phase transition. Comparing the fit residuals for the various models we find only magnetic structures within the Γ_5 irrep produce reasonable fits. Of those, the magnetic space group $P2_1^{'}2_1^{'}2$ produces the lowest fit residuals with similar quality to our known zero field structure [the calculated and observed intensities are shown in Fig. 7(c)]. Using this model, we obtain a magnetic moment of 7.7(4) μ_B/Er for the 4 T structure, which is similar to the 8.1(3) μ_B/Er obtained in the zero-field structure within the certainty of our measurements. We note that because of the limited number of peaks, we did not attempt modeling with the Γ_5 $P2_2^{'}$ structure for the same reasons previously discussed for the powder modeling.

Considering the 1 T data, we obtain similar results albeit with larger residuals. As seen in Figs. 6(d) and 6(c), at 1 T there is still intensity on the (100) and (001) reflections, which is gone by 4 T. This may indicate that the phase transition is not complete at this intermediate field, possibly due to small misalignments of our coaligned crystals, which results in some remnant of the sample remaining in the zero-field magnetic structure. Nonetheless, the $P2_1^{'}2_1^{'}2$ structure produces the lowest fit residuals for both the 1 and 4 T data.

Figure 8 shows both the 0 and 4 T magnetic structures determined using the single-crystal data. Comparing these reveals an interesting similarity—they are nearly identical save for an inversion of moments with components anti parallel to the applied field about their crystallographic position. The left panels of Fig. 8 show this more clearly by focusing on a single pair of edge-sharing Er_4 triangles. Each Er_4 unit has three distinct bond lengths labeled $b_1 = 3.57(1)$, $b_2 = 3.60(1)$, and $b_3 = 3.80(1)$, with the latter two defining the sides of the unit and b_1 the shared edge internal to the Er_4 unit. As previously discussed, along the short b_1 the Er moments are coaxial with the bond, this is seen in both the 0 and 4 T structures. Considering the full unit cell, this Er_4 unit forms the Er sublattice by connecting via a corner along the long axis to another Er_4 unit's short axis (i.e., b_1). In this way, every Er is part of the short axis of an Er_4 unit and has its moment subject to the local Ising behavior—always aligning with b_1.

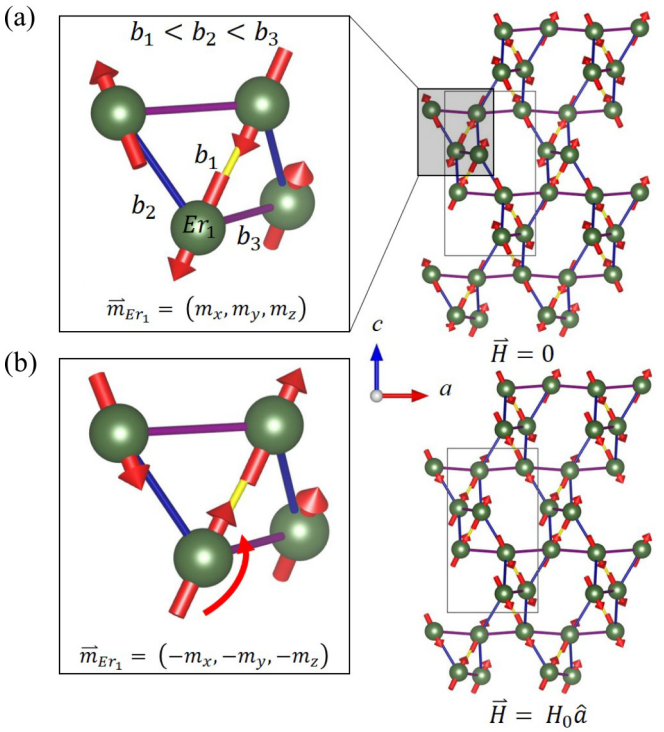

FIG. 8. Best fit magnetic structure for the (a) 0 and (b) 4 T data (with field applied along the a axis. For each model, a zoomed-in region of the Er sublattice is shown emphasizing the geometry of the edge-sharing Er triangles. The labels b_1, b_2, and b_3 refer to the three different Er-Er distances within each pair of edge sharing Er triangles. The label Er_1 only refers to this figure for the purpose of describing the inversion of the magnetic moment. The b_1 short Er-Er distance is denoted by a yellow bar while the longer b_2 and b_3 distances are denoted by blue and purple bars, respectively. This allows for the short Er-Er distance to be seen easily throughout the structure models.

In the applied field, the Er_4 may be divided into two sets—one with the a component of the b_1 Er aligned with the field, the other with the a component of the b_1 Er antiparallel. In the latter, there exists competition between the energetically unfavorable field alignment and the strong local anisotropy fixing the moment to the b_1 direction. As the field is increased, the antiparallel moments invert reducing the misalignment with the applied field while not breaking from the easy axis. Remarkably, Er moments which have no component antiparallel to the field appear unaffected within the statistical certainty of our measurement.

It is significant that we observe complete inversion of the antiparallel moments as it indicates a strong anisotropy which keeps the moment locked to a certain axis. Such a response to the applied field describes a class I MMT [44]. Class I MMTs, or spin-flip transitions, are characterized by a strong local anisotropy on the magnetic site which prevents the moment from rotating away from the easy axis (i.e., spin-flop) in response to the applied field. In class I MMTs, the anisotropy requires the moment to be either parallel or anitparallel to the easy axis. Consequently, once a critical field is reached (H_c), the material undergoes a first-order phase transition to a ferrimagnetic or paramagnetic state (the details of the HvT

phase diagram are variable but at low temperatures the MMT is discontinuous) [44]. This is exactly what is shown in our analysis.

To corroborate this classification, we can attempt to characterize the order of the observed MMT transition. While the most straightforward route would be to consider the peak intensities as the magnetic order parameter (Intensity $\propto M^2$) unfortunately, the order parameter scans shown in Figs. 6(b) and 6(c) are not reliable in this regard due to low data-point density and powder origin. However, symmetry considerations of the magnetic structures are helpful. The change from the zero-field (Γ_3) irrep to the in-field structure of Γ_5 is not a continuous transition, in which case we would expect one irrep or an associated basis vector to develop a finite value. Rather, what we see is a change in irreps, where one irrep cannot smoothly evolve into the other. From this, we can determine that the transition is of first-order in agreement with the general theory of class I MMTs.

We note that the manifestation of the MMT in $Er_2Ge_2O_7$ is interesting—in most metamagnets, the magnetic moments exhibit a single universal easy axis leading to colinear or coplanar magnetic structures. This is the case of the zero-field structure of $Ho_2Ge_2O_7$ and presumably $Dy_2Ge_2O_7$, yet no MMT has been reported in either of these materials. In contrast, the R moments in $Er_2Ge_2O_7$ exhibit a spiral structure with significant out-of-plane canting. We propose that this may be due to the change in f-orbital shape from oblate in Ho and Dy to prolate in Er, which suggests an easy-plane behavior for the former two rather than the easy-axis behavior of the latter. This strong axial anisotropy of $Er_2Ge_2O_7$ may lead to an intermediate magnetic phase where the applied field has overcome only some of the terms in the Hamiltonian (such as the exchange interactions) and is not yet strong enough to overcome the easy axis anisotropy. Meanwhile the easy-plane of $Ho_2Ge_2O_7$ and $Dy_2Ge_2O_7$ may allow for a rotation into a paramagnetic state without a discrete intermediate magnetic structure as indicated by specific heat measurements in Ref. [28]. However, the complete magnetic Hamiltonians of all three compounds are needed to fully understand the different behaviors of these systems, which is outside the scope of this paper. Nevertheless, the canted moment observed here in $Er_2Ge_2O_7$ is a special case of MMT [45].

Furthermore, we notice a similarity to the spin-ice materials in the presence of a MMT with a relatively low critical field of $H_c < 1$ T (compared to $H_c \gg 1$ T seen in many metamagnetic materials) [14,44,46–48]. In $Ho_2Ti_2O_7$, a similar $H_c \sim 0.3$ T and strong local anisotropy were observed. In this canonical spin-ice, the MMT revealed the competition between FM exchange and single-ion anisotropy with the low-field overcoming the exchange interaction—giving important information about the underlying physics. More broadly, in the spin-ice pyrochlores, the MMT from an unordered zero-field state to a magnetically ordered state in applied fields is intimately related to the physics being a manifestation of a liquid-gas transition of emergent magnetic monopoles [16]. While the behavior we report here is different, having a fully ordered AFM ground state, the similarities in MMT indicate similar competing interactions.

Indeed, in further analogy here we also find the easy axis is determined locally [14–16]. This is a vital component in the pyrochlores to the establishment of the frustrating ice rules. Interestingly, the RPG structure is ostensibly tunable—related to the more usual planar spiral structure exhibited in both $Ho_2Ge_2O_7$ and $Dy_2Ge_2O_7$ only by changing the R. Whether this is an effect of the smaller ionic size—which, as discussed previously, results in shorter R-R distances and therefore presumably stronger magnetic dipole interactions—of affected bond angles and exchange interactions, changes in the magnetic properties of the R ion due to different spin-quantum numbers, resultant changes to the crystal field levels, or combinations of all of these effects is unknown and warrants continued study. Determining how to tune these parameters to increase the frustration in these RPG is of great interest to possibly find a new system with spin-ice or spin-liquid physics—especially in light of the previous work, which has shown the spins to be Ising-like and dynamic susceptibilities reminiscent of spin-freezing physics [28,29].

IV. CONCLUSIONS

We have reported on neutron-diffraction studies elucidating the zero-field and field-dependent low-temperature magnetic structures of RPG $Er_2Ge_2O_7$. In zero field, we find magnetic ordering at $T_N = 1.15$ K, which together with a $\theta_w = -14.4$ K indicates a relatively strong frustration index of $f \sim 13$. All magnetic reflections can be indexed with a $k = (0, 0, 0)$ AFM structure and modeled well by magnetic space group symmetry $P4_1'2_12'$ with Er moments of $m = 8.1\mu_B$ aligned along the short Er-Er distance of the R sublattice. Field-dependent studies reveal a MMT with a critical field of $H_c \sim 0.5$ T at 0.5 K, which is stable up to applied fields of 4 T. This second magnetic structure maintains $k = (0, 0, 0)$ but with a spin reorientation to magnetic space group symmetry $P2_1'2_1'2$ driven by an inversion of Er sites with magnetic moment components antiparallel to the applied field. Symmetry analysis of these two structures indicates the field-driven transition as a first-order class I spin-flip MMT characteristic of a strong local anisotropy at the magnetic site. Together the observations of a local easy axis along the short Er-Er distance and a spin-flip transition encourage a local-Ising-type description of the magnetic order in which each Er moment aligns either spin-up or spin-down along this local easy axis.

The observation of both a MMT and local Ising behavior indicates physics analogous to the spin-ice pyrochlores in a considerably different R sublattice. In many of the spin-ice pyrochlores, such metamagnetic transitions have been observed but from paramagnetic to FM rather than from AFM to ferrimagnetic as seen here. In those systems, such a transition is interpreted as the tunable gas-liquid transition of magnetic monopoles. While such a situation is not the case in $Er_2Ge_2O_7$, the spin-flip transition is evidence of strong anisotropy and quantum behavior as the spins are locked along discrete directions and can be tuned selectively between spin-up and spin-down states with an applied field. This observation encourages further work looking to explicate the spin Hamiltonian. Such understanding may lead to new ways to tune the magnetic structure—either gaining finer control over the individual spin states or possibly increasing the frustration and achieving a spin-ice state. Such work is of potential

interest in the search for new materials with exotic quantum ground states such as spin-liquids.

ACKNOWLEDGMENTS

This research used resources at the High Flux Isotope Reactor, a DOE Office of Science User Facility operated by the Oak Ridge National Laboratory. The research is partly supported by the DOE, Office of Science, Basic Energy Sciences (BES), Materials Science and Engineering Division. Work performed at Clemson University was funded by DOE BES Grant No. DE-SC0014271.

[1] G. H. Wannier, Phys. Rev. **79**, 357 (1950).
[2] B. Derrida, J. Vannimenus, and Y. Pomeau, J. Phy. C: Solid State Phys. **11**, 4749 (1978).
[3] A. Ramirez, Annu. Rev. Mater. Sci. **24**, 453 (1994).
[4] J. S. Gardner, M. J. P. Gingras, and J. E. Greedan, Rev. Mod. Phys. **82**, 53 (2010).
[5] R. Harris, Y. Sato, A. J. Berkley, M. Reis, F. Altomare, M. H. Amin, K. Boothby, P. Bunyk, C. Deng, C. Enderud, S. Huang, E. Hoskinson, M. W. Johnson, E. Ladizinsky, N. Ladizinsky, T. Lanting, R. Li, T. Medina, R. Molavi, R. Neufeld, T. Oh, I. Pavlov, I. Perminov, G. Poulin-Lamarre, C. Rich, A. Smirnov, L. Swenson, N. Tsai, M. Volkmann, J. Whittaker, and J. Yao, Science **361**, 162 (2018).
[6] A. Kitaev, Ann. Phys. **303**, 2 (2003).
[7] A. Banerjee, C. Bridges, J.-Q. Yan, A. Aczel, L. Li, M. Stone, G. Granroth, M. Lumsden, Y. Yiu, J. Knolle *et al.*, Nat. Mater. **15**, 733 (2016).
[8] A. Banerjee, J. Yan, J. Knolle, C. Bridges, M. Stone, M. Lumsden, D. Mandrus, D. Tennant, R. Moessner, and S. Nagler, Science **356**, 1055 (2017).
[9] N. Ma, Phys. B: Condens. Matter **512**, 100 (2017).
[10] B. Zhang, P. Baker, Y. Zhang, D. Wang, Z. Wang, S. Su, D. Zhu, and F. Pratt, J. Am. Chem. Soc. **140**, 122 (2018).
[11] J. Zheng, K. Ran, T. Li, J. Wang, P. Wang, B. Liu, Z.-X. Liu, B. Normand, J. Wen, and W. Yu, Phys. Rev. Lett. **119**, 227208 (2017).
[12] S.-H. Do, S.-Y. Park, J. Yoshitake, J. Nasu, Y. Motome, Y. Kwon, D. Adroja, D. Voneshen, K. Kim, T.-H. Jang *et al.*, Nat. Phys. **13**, 1079 (2017).
[13] C. Balz, B. Lake, J. Reuther, H. Luetkens, R. Schönemann, T. Herrmannsdörfer, Y. Singh, A. Islam, E. Wheeler, J. Rodriguez-Rivera *et al.*, Nat. Phys. **12**, 942 (2016).
[14] M. J. Harris, S. T. Bramwell, D. F. McMorrow, T. Zeiske, and K. W. Godfrey, Phys. Rev. Lett. **79**, 2554 (1997).
[15] H. Fukazawa, R. G. Melko, R. Higashinaka, Y. Maeno, and M. J. P. Gingras, Phys. Rev. B **65**, 054410 (2002).
[16] C. Castelnovo, R. Moessner, and S. Sondhi, Nature **451**, 42 (2008).
[17] R. Siddharthan, B. S. Shastry, A. P. Ramirez, A. Hayashi, R. J. Cava, and S. Rosenkranz, Phys. Rev. Lett. **83**, 1854 (1999).
[18] S. Bramwell and M. Harris, J. Phys.: Condens. Matter **10**, L215 (1998).
[19] S. Bramwell and M. Gingras, Science **294**, 1495 (2001).
[20] J. E. Greedan, J. Alloys Compd. **408–412**, 444 (2006), Proceedings of Rare Earths'04 in Nara, Japan.
[21] C. Krey, S. Legl, S. R. Dunsiger, M. Meven, J. S. Gardner, J. M. Roper, and C. Pfleiderer, Phys. Rev. Lett. **108**, 257204 (2012).
[22] Z. Hiroi, K. Matsuhira, S. Takagi, T. Tayama, and T. Sakakibara, J. Phys. Soc. Jpn. **72**, 411 (2003).
[23] H. Cao, A. Gukasov, I. Mirebeau, P. Bonville, C. Decorse, and G. Dhalenne, Phys. Rev. Lett. **103**, 056402 (2009).
[24] H. Cao, A. Gukasov, I. Mirebeau, P. Bonville, and G. Dhalenne, Phys. Rev. Lett. **101**, 196402 (2008).
[25] S. V. Isakov, K. S. Raman, R. Moessner, and S. L. Sondhi, Phys. Rev. B **70**, 104418 (2004).
[26] B. C. den Hertog and M. J. P. Gingras, Phys. Rev. Lett. **84**, 3430 (2000).
[27] U. Becker and J. Felsche, J. Less-Common Met. **128**, 269 (1987).
[28] E. Morosan, J. A. Fleitman, Q. Huang, J. W. Lynn, Y. Chen, X. Ke, M. L. Dahlberg, P. Schiffer, C. R. Craley, and R. J. Cava, Phys. Rev. B **77**, 224423 (2008).
[29] X. Ke, M. L. Dahlberg, E. Morosan, J. A. Fleitman, R. J. Cava, and P. Schiffer, Phys. Rev. B **78**, 104411 (2008).
[30] M. Ghosh, S. Jana, D. Ghosh, and B. Wanklyn, Solid State Commun. **107**, 113 (1998).
[31] J. Snyder, J. Slusky, R. Cava, and P. Schiffer, Nature **413**, 48 (2001).
[32] J. Snyder, B. G. Ueland, J. S. Slusky, H. Karunadasa, R. J. Cava, and P. Schiffer, Phys. Rev. B **69**, 064414 (2004).
[33] G. Ehlers, A. Cornelius, T. Fennell, M. Koza, S. Bramwell, and J. Gardner, J. Phys.: Condens. Matter **16**, S635 (2004).
[34] G. M. Sheldrick, Acta Crystallogr. Sect. C **71**, 3 (2015).
[35] J. Rodríguez-Carvajal, Phys. B: Condens. Matter **192**, 55 (1993).
[36] L. W. Finger, D. E. Cox, and A. P. Jephcoat, J. Appl. Cryst. **27**, 892 (1994).
[37] A. Wills, Phys. B: Condens. Matter **276–278**, 680 (2000).
[38] B. J. Campbell, H. T. Stokes, D. E. Tanner, and D. M. Hatch, J. Appl. Crystallogr. **39**, 607 (2006).
[39] J. Appl. Crystallogr. **44**, 1272 (2011).
[40] R. D. Shannon, Acta Crystallogr. Sect. A **32**, 751 (1976).
[41] R. Moon, J. Phys. Colloques **43**, C7-187 (1982).
[42] See Supplemental Material at http://link.aps.org/supplemental/10.1103/PhysRevMaterials.3.014405 for additional information related to the symmetry analysis.
[43] L. Balents, Nature **464**, 199 (2010).

[44] E. Stryjewski and N. Giordano, Adv. Phys. **26**, 487 (1977).
[45] Y. Kitano and T. Nagamiya, Prog. Theor. Phys. **31**, 1 (1964).
[46] M. Deppe, S. Lausberg, F. Weickert, M. Brando, Y. Skourski, N. Caroca-Canales, C. Geibel, and F. Steglich, Phys. Rev. B **85**, 060401 (2012).
[47] C. P. C. Medrano, D. C. Freitas, E. C. Passamani, C. B. Pinheiro, E. Baggio-Saitovitch, M. A. Continentino, and D. R. Sanchez, Phys. Rev. B **95**, 214419 (2017).
[48] R. Sibille, E. Lhotel, M. C. Hatnean, G. Balakrishnan, B. Fåk, N. Gauthier, T. Fennell, and M. Kenzelmann, Phys. Rev. B **94**, 024436 (2016).